

AAE 520
EXPERIMENTAL AERODYNAMICS
Professor Joe Jewell

Experiment 3 Report:
SHOCKWAVE – BOUNDARY LAYER INTERACTIONS
AT MACH 2.0

Purdue University
School of Aeronautics and Astronautics

By: Suzanne Swaine and Terry Zhou

Spring 2022

1. Abstract

Shockwave-boundary layer interaction of Mach 2 flow over a 20° ramp was studied using pressure measurements and Schlieren-based optical flow visualization techniques. The separated oblique shock, caused by the large ramp angle, presented oscillation in the separation bubble upstream. Attempts were made to characterize this oscillation using Fast Fourier Transformation. Furthermore, Shadowgraphy and Schlieren imaging were performed using a DSLR. The shutter speed and ISO settings were balanced to provide the sharpest freeze frame image of the flow while still providing sufficient illumination. Results clearly demonstrate the oblique shock and its unsteadiness.

2. Introduction

Supersonic flight has been of interest in the past decades. The ability to travel in speeds beyond the speed of sound requires multi-disciplinary efforts. Designs of supersonic vehicles require deep understanding of aerodynamics phenomena absent in subsonic conditions. In supersonic flows, the turning of the flow presents more complexity than in subsonic flows. Since information cannot travel faster than the flow itself, the turning of the high-speed flow into itself generally induces oblique shocks. As a result, the supersonic flow around a finite length of concave surface presents both two-dimensional and three-dimensional behaviors.

In order to study these complicated two-dimensional and three-dimensional flows in supersonic conditions, more simplified models have been developed to study the specific interactions. This experiment aims to investigate the 2D and 3D behavior of ramp flow in Mach 2 settings. The ramp angle exceeds the maximum turning angle which would allow an oblique shock to stay attached, thus creating unsteady shockwave boundary layer interactions. Pressure measurements and flow visualizations are to be performed to both qualitatively and quantitatively characterize the oblique shocks and expansion fans present in the ramp flow.

3. BACKGROUND

3.1. THEORY

3.1.1. Shockwaves

When supersonic flow encounters a concave corner with angle θ and flow is forced to turn into itself to stay tangent to the wall, an oblique shockwave is formed, as seen in Figure 1. Across the shock, the pressure, Mach number, density, and temperature all experience a discontinuous change (Mach number decreases, the other three properties increase).

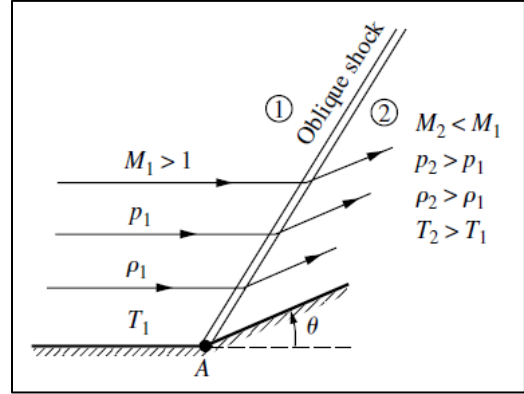


Figure 1. Supersonic flow over a concave corner [1]

For every Mach number, there is a maximum turning angle, θ_{\max} at which the oblique shockwave will detach from the corner and the shockwave will take on a more curved shape, as depicted in Figure 2.

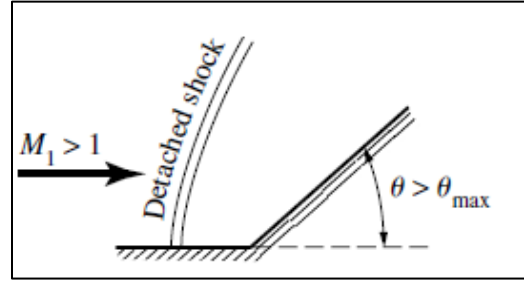


Figure 2. A detached shockwave upstream of a concave corner with $\theta > \theta_{\max}$ [1]

The specific relationship between θ (turn angle), β (oblique shock angle), and Mach number is:

$$\tan(\theta) = 2 \cot(\beta) \frac{M_1^2 \sin^2 \beta - 1}{M_1^2 (\gamma + \cos 2\beta) + 2}$$

where γ indicates the heat capacity ratio of the fluid. Due to the nonlinear behavior shown in the above relationship, there are two shock solutions for each Mach number, classifying the oblique shocks as strong and weak (see Figure 3). Strong shocks can be identified by their larger wave angles, and the Mach number downstream of a strong shock will be always be subsonic. Typically, all attached shocks are weak shocks. Weak shocks may have slightly subsonic downstream Mach numbers if the θ is close to the θ_{\max} for the given shock number.

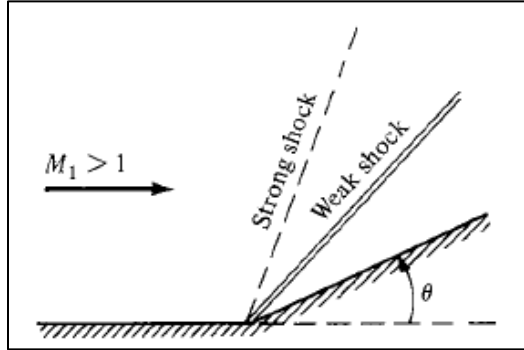


Figure 3. Strong vs weak shockwave geometry [1]

3.1.2. Expansion Fans

When supersonic flow encounters a convex corner (as depicted in Figure 4), once again the flow at the wall is forced to remain tangent to the

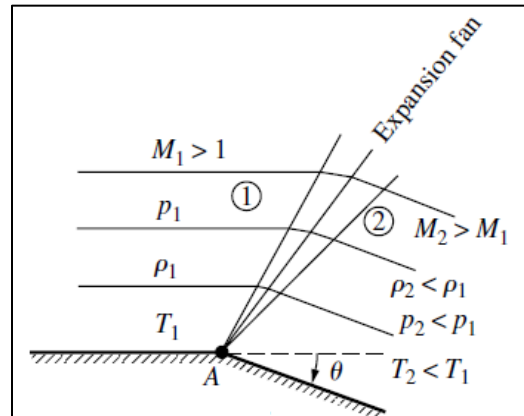


Figure 4. Supersonic flow over a convex corner [1]

wall and the streamlines nearest the wall are deflected down at an angle of θ , expanding the flow.

Unlike shockwaves, the pressure, Mach number, density, and temperature do not experience a step change, but instead change continuously across the expansion fan. The Prandtl-Meyer function is defined as the following and can be used to determine the resulting Mach number after the expansion:

$$v(M) = \int \frac{\sqrt{M^2 - 1}}{1 + \frac{\gamma - 1}{2} M^2} \frac{dM}{M}$$

where M is the Mach number

$$v(M) = \sqrt{\frac{\gamma + 1}{\gamma - 1}} \arctan \sqrt{\frac{\gamma - 1}{\gamma + 1} (M^2 - 1)} - \arctan \sqrt{M^2 - 1}$$

where γ is the specific heat ratio

$$\theta = v(M_2) - v(M_1)$$

This process is isentropic and thus the quantities can be related as the following:

$$\frac{T_2}{T_1} = \left(\frac{1 + \frac{\gamma - 1}{2} M_1^2}{1 + \frac{\gamma - 1}{2} M_2^2} \right) \quad \frac{p_2}{p_1} = \left(\frac{1 + \frac{\gamma - 1}{2} M_1^2}{1 + \frac{\gamma - 1}{2} M_2^2} \right)^{\frac{\gamma}{\gamma - 1}} \quad \frac{T_2}{T_1} = \left(\frac{1 + \frac{\gamma - 1}{2} M_1^2}{1 + \frac{\gamma - 1}{2} M_2^2} \right)^{\frac{1}{\gamma - 1}}$$

where T is the temperature, p is the pressure. subscript 1 denotes upstream conditions and 2 denotes downstream conditions

3.1.3. Converging-Diverging Nozzles

Within a nozzle flow, the area-velocity relation is the following:

$$\frac{dA}{A} = (M^2 - 1) \frac{du}{u}$$

where A denotes the area and u denotes the velocity

This equation can be considered in both subsonic and supersonic conditions. In subsonic conditions, when area gradient is negative, i.e., the area is decreasing, the velocity experiences a positive gradient. This is analogous to Bernoulli's Equation where flow speeds up when the cross-sectional area is decreasing in order to maintain consistent flow rate. However, in supersonic conditions, the opposite can be observed. Velocity experiences a positive gradient only when area is also increasing.

The opposite behavior in the two flow conditions allow for the design of converging-diverging nozzles where the flow is initially subsonic. Through the converging section, the subsonic flow speeds up and eventually achieves sonic condition at the end of this section. From there, the sonic flow is expanded into the diverging section, through the test section. The specific

Mach number of the test section can be designed based on the above area-velocity relation. Note that in order to start the converging-diverging nozzle (i.e., to achieve supersonic conditions in the diverging section), the flow must be choked at the throat where the mass flow rate is held constant and can no longer increase.

3.1.4. Shockwave-Boundary Layer Interaction (SWBLI)

When a ramp subjected to supersonic flow has a high enough angle, the adverse pressure gradient becomes strong enough to separate the upstream boundary layer. Doing so traps a small separation bubble where the fluid within does not convect downstream, known as a closed shockwave boundary layer interaction. The separation length scale denoted as L_{sep} increases with increasing ramp angle. As a result, the separation bubble also increases in size. The flow is then lifted and convects downstream above the bubble. The base of the resulting separation shock is the shock foot. The shock foot oscillates back and forth over an intermittent region which causes pressure fluctuations along the upstream region of the ramp [2]. Similar work in the past by Erenil and Dolling [3] indicated that the oscillations within the intermittent region exhibit a dominant frequency of approximately 500 Hz [2].

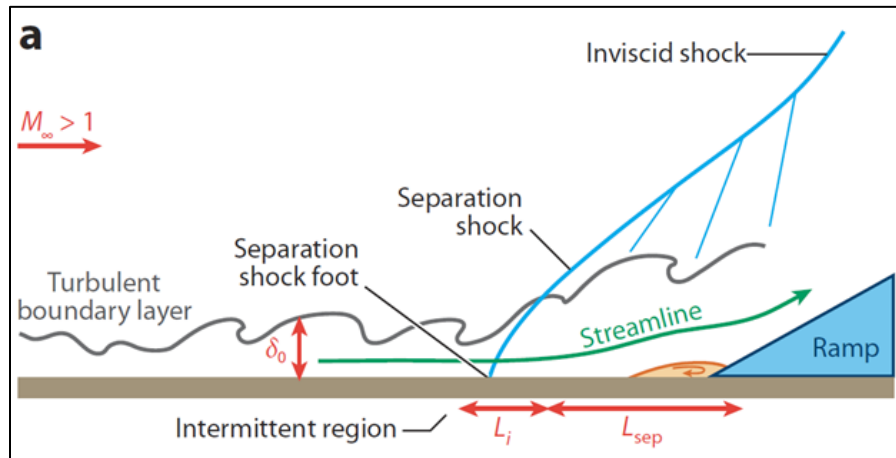


Figure 5. Schematic of shockwave boundary layer interaction of supersonic flow over ramp [2]

3.1.5. Schlieren Imaging

Refraction is the phenomenon in which light waves traveling through mediums of different densities change direction. Schlieren imaging, invented by August Toepler in 1864 [4] uses refraction principles to capture photographs of density variations (the first derivative of density) in fluid flows. These images can be used to study the flow behavior and are particularly popular for studying shockwaves and expansion fans. A typical Schlieren imaging setup consists of a light source, small aperture, several curved mirrors (or lenses), a knife edge, a camera, and certainly the fluid flow to be studied.

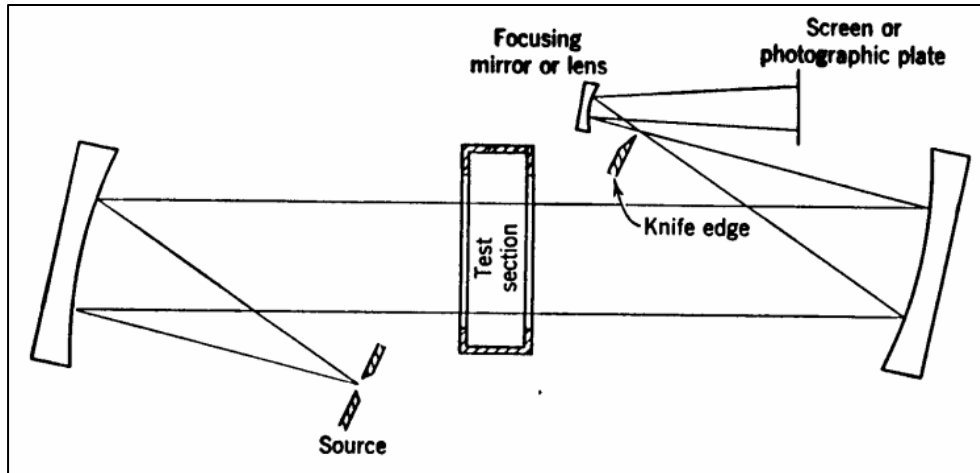


Figure 6. Schematic of a Schlieren imaging setup [5]

To collimate the light from a single point, the light source is located behind the small aperture. The light travels through the aperture, the collimating mirror, and through the fluid flow (e.g., wind tunnel test section) where variations in density refract portions of the light. A lens or curved mirror is used to focus the collimated light, and the knife edge is placed at the focus point in such a way that a portion of the light is blocked. The remainder of the light then travels to a camera to be photographed. As shown in Figure 7, the knife edge will cause the refracted image to show as darker or lighter depending on the density gradient.

The orientation of the knife edge is important, as gradients perpendicular to the knife edge will be captured with greater sensitivity. Two knife edges in different orientations can also be used to increase the sensitivity of the imaging system to gradients in multiple directions. As an alternative to a knife edge, a prism or color filter can be used to create colored Schlieren images, though this was not attempted for the experiments outlined in this report.

The clearest Schlieren images are those of perfectly steady flow, as turbulence or unsteadiness may result in blurring. One mitigation method is to increase the shutter speed and/or to use a very short, very bright flash of light rather than a continuous source. A similar consideration is that the sensitivity of the Schlieren can be increased by blocking larger amounts

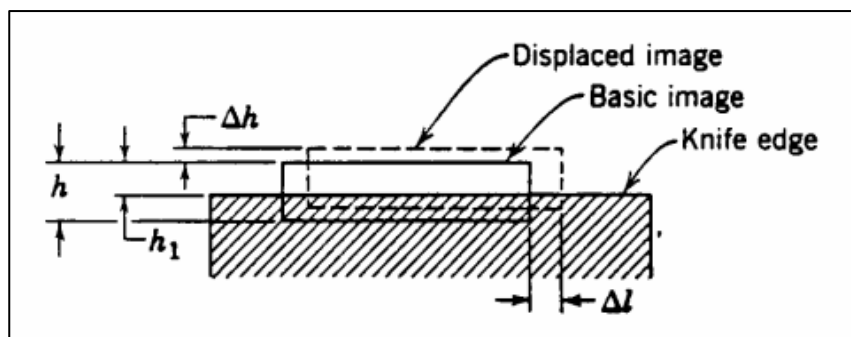


Figure 7. Density variations cause the light to refract unevenly, resulting in a "basic image" and a "displaced image" which are then partially blocked by the knife edge [5]

of the light with the knife edge, but sufficient light is still required for the image so the brightness of the light source may constrain the sensitivity of the images.

The Gladstone-Dale Relation and Fermat's Equation, as shown below, can be coupled to fully describe the underlying working principle of Schlieren and other Schlieren-based techniques.

$$n = 1 + K\rho$$

where K is the Gladstone-Dale Constant ($= 0.2 \times 10^{-3} \frac{m^3}{kg}$ for air) and n is the refractive index of the flow medium

$$\frac{d}{d\xi} \left(n \frac{dx}{d\xi} \right) = \nabla n$$

3.1.6. Shadowgraphy

Shadowgraphy requires a nearly identical setup to the one required for Schlieren imaging, and works on similar principles. The most significant difference between the two is that shadowgraphy captures the second derivative of density rather than the first as it does not use a knife edge to introduce diffraction. As a result, Shadowgraphy is not nearly as sensitive as Schlieren. However, in circumstances such as oblique shocks and normal shocks where the flow feature is strong and contains high contrast, shadowgraphy is better suited to exclude noise and smearing of the flow features.

3.2. Equipment

3.2.1. Supersonic Wind Tunnel

Figure 8 shows a diagram of the supersonic wind tunnel used for these experiments.

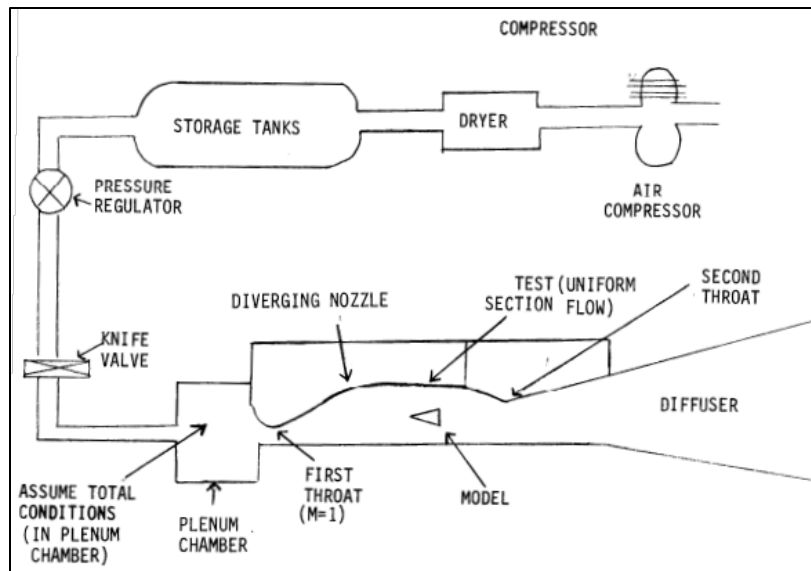


Figure 8. Supersonic wind tunnel schematic [6]

The wind tunnel has a 250 ft³ storage tank that contains compressed, dried air. The air travels downstream from the storage tank through a pressure regulator, and then through a knife valve. This knife valve allows an operator to quickly start and stop the airflow in the tunnel. A plenum chamber is used to reduce turbulence in the flow, and the velocity is reduced to a negligible velocity so that total and static conditions are assumed to be equal. After the plenum chamber, the flow encounters a converging-diverging nozzle, the first throat in the tunnel. This nozzle accelerates the subsonic flow to sonic conditions at the throat (Mach = 1.0) and supersonic conditions beyond the throat and through the test section. The sonic condition at the throat was used as a point of reference for other measurements throughout the experiment. Because of the fixed geometry of the throat, the flow velocity in the tunnel when using this nozzle is always Mach 2.0.

Downstream of the test section is the second throat in the wind tunnel. This throat serves to decelerate the flow and control the location of the subsequent shockwave. There is a vacuum pump located downstream capable of reducing the downstream pressure, i.e., exit pressure, if a larger pressure delta is desired, though the tunnel can also be vented to the atmosphere.

Although Mach number is strictly based on the designed area ratio, Reynolds number depends on other flow conditions which include total upstream pressure, as seen in equations below. When the tunnel is operating under vacuum in the downstream, the required upstream pressure can be decreased while still choking the flow at the throat, effectively starting the tunnel but operating at lower Reynolds number than when vented to the atmosphere.

$$\frac{A}{A^*} = \left(\frac{\gamma + 1}{2}\right)^{-\frac{\gamma+1}{2(\gamma-1)}} \frac{\left(1 + \frac{\gamma-1}{2} M^2\right)^{\frac{\gamma+1}{2(\gamma-1)}}}{M}$$

where A is the area, γ is the specific heat ratio, and M is the Mach number

$$\frac{Re}{L} = \frac{p_0 a_0}{RT_0 \mu_0} M \left(1 + \frac{\gamma-1}{2} M^2\right)^{0.268 - \frac{1}{\gamma-1}}$$

Where Re is the Reynolds number, L is the characteristic length, p_0 is the total upstream pressure, a_0 is the isentropic speed of sound, R is the ideal gas constant, T_0 is the total upstream temperature, μ_0 is the isentropic viscosity, and M is the Mach number

For this experiment, a pressure tapped block with a 20° ramp was inserted into the test section and results were collected for both downstream conditions. Though only results of vacuumed downstream were discussed.

3.2.2. Pressure Sensors and Oscilloscope

The diverging nozzle and test section of the supersonic wind tunnel is outfitted with pressure taps allowing Kulite pressure sensors to be connected. These pressure sensors are connected to a pressure transducer which in turn sent the AC and/or DC signals to an oscilloscope (Tektronix MDO3024, 100 MHz, 2.5 GS/s) so that the data can be observed in real time and saved for later analysis.

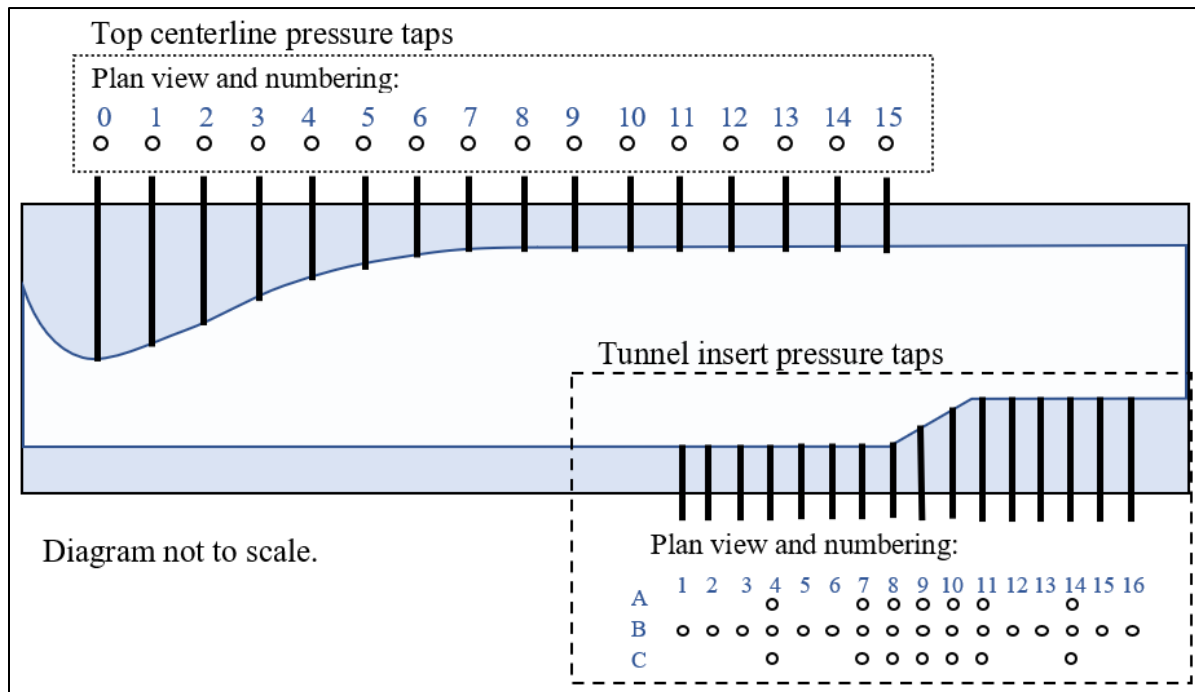


Figure 9. A not-to-scale diagram depicting the arrangement of pressure taps in the wind tunnel

16 pressure ports exist along the top centerline of the wind tunnel. The ports are evenly spaced with 1.0 inches between them, with the most upstream port (Location 0) located at the first throat. 30 pressure ports exist on the ramp tunnel insert with 16 located along the centerline. Figure 9 shows a not-to-scale diagram of the pressure tap arrangement along the top centerline and in the tunnel insert with 20° ramp.

3.2.3. Imaging Setup

The equipment used for the Schlieren and shadowgraphy imaging closely resembled the setup described in the Background Section 3.1.5. text. The light was generated by an LED light source and directed through a pinhole and reflected off the curved collimating mirror through the 3" Schlieren grade windows located on either side of the wind tunnel test section (see Figure 10). On the other side of the test section was a second curved mirror which focused the light to a point. For Schlieren imaging, a knife edge was mounted at this focus point and oriented in such a way as to block approximately half of the light (see Figure 11 and 12). For shadowgraphy, no knife edge was used. A flat mirror was used to redirect the light, through an imaging lens, into the Canon DSLR camera; the flat mirror was not necessary for the Schlieren or shadowgraphy setups but was required because of geometry constraints. Note that lenses of different focal lengths could be used in place of the imaging lens to achieve various field of view, and in turn, spatial resolution.

4. PROCEDURE

4.1. Kulite Pressure Sensor Calibration

Before running the wind tunnel, the eight Kulite pressure sensors were calibrated by attaching them to a vacuum tank with known pressure. Note that eight were calibrated, but only sensors 1 through 7 were used throughout the experiments as sensor 8 was known to be faulty. Pressure in the tank was recorded manually, from the readings of an electrical pressure gauge, and the oscilloscope was used to record the voltage outputs from the Kulites. A valve was used to incrementally increase the pressure in the tank from as low as 25 Torr up to

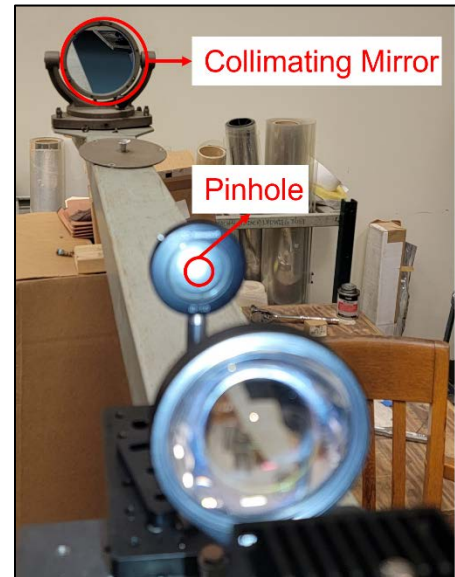


Figure 10. Collimating mirror and pinhole

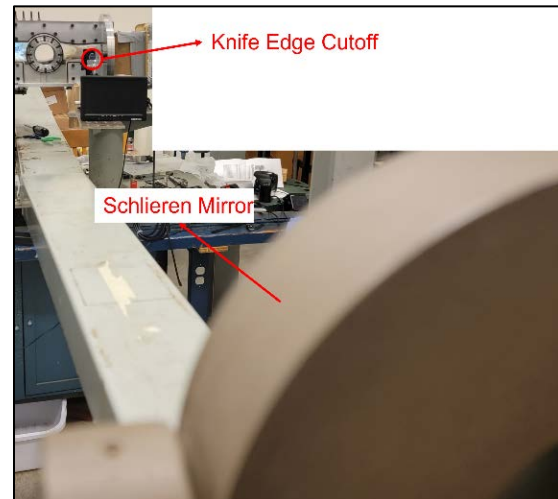


Figure 11. Support arm for the Schlieren mirror

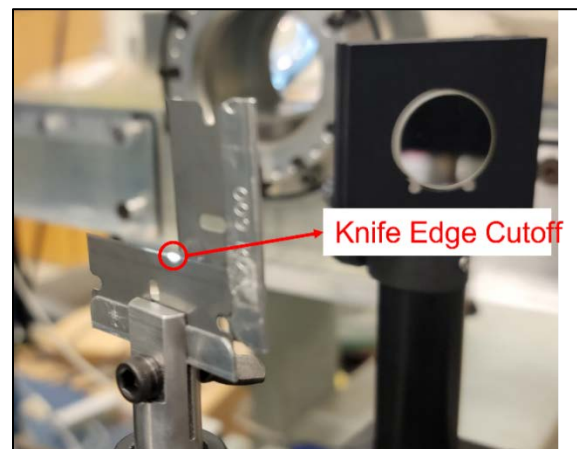


Figure 12. Knife edge consisting of two razor blades oriented vertically and horizontally

approximately 752 Torr (~1 atm). The results of this calibration are presented in Section 5.1.

4.2. Operation of the Tunnel

The tunnel was operated on shop air within the building. In order to accurately control the total upstream pressure, a pressure regulator, suitable for up to 80 psia, was used upstream of the converging-diverging nozzle. A pressure knife valve inline between the regulator and the nozzle was used to control the operation of the tunnel. This was verified by the presence of the oblique shock in the Schlieren images captured. When venting into vacuum, the test article was prepared and set in place before plumbing of the vacuum pump was manipulated to pull vacuum in the vacuum tank.

4.3. Nozzle Characterization

Two configurations were tested in order to characterize the flow within the diverging nozzle. The seven functioning pressure sensors were installed on alternating pressure taps along the top centerline of the diverging nozzle for Configuration 1, and then were shifted by one tap for Configuration 2. Sensor #1 remained on Tap 0 for the duration of the experiment so the throat pressure could be used as a reference point. Figure 13. Top centerline pressure taps used for Configuration 1 (blue and green) and Configuration 2 (yellow and green). shows the pressure taps highlighted in blue and green representing Configuration 1, and the pressure taps highlighted in yellow and green representing Configuration 2.

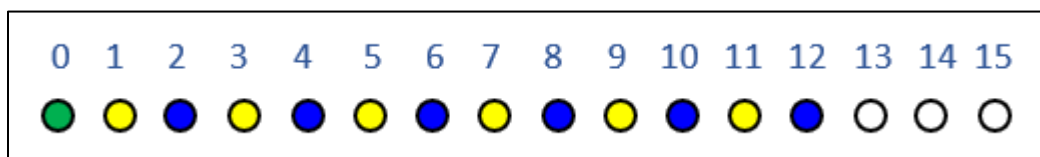


Figure 13. Top centerline pressure taps used for Configuration 1 (blue and green) and Configuration 2 (yellow and green).

For each configuration, the knife valve was used to open the flow on the tunnel for approximately 2-3 seconds per test point, during which time the oscilloscope was used to record the DC voltages from the seven pressure taps. Ten test points were recorded for every configuration.

4.4. Ramp Characterization

Three configurations were tested in order to characterize the flow within the test section, as the flow encountered the 20° ramp and shockwaves as well as expansion fans were present. For all configurations, pressure sensor #1 remaining at the throat of the tunnel to serve as a reference point. The remaining 6 sensors were arranged as shown in Figure 14 for Configuration 3 (blue), 4

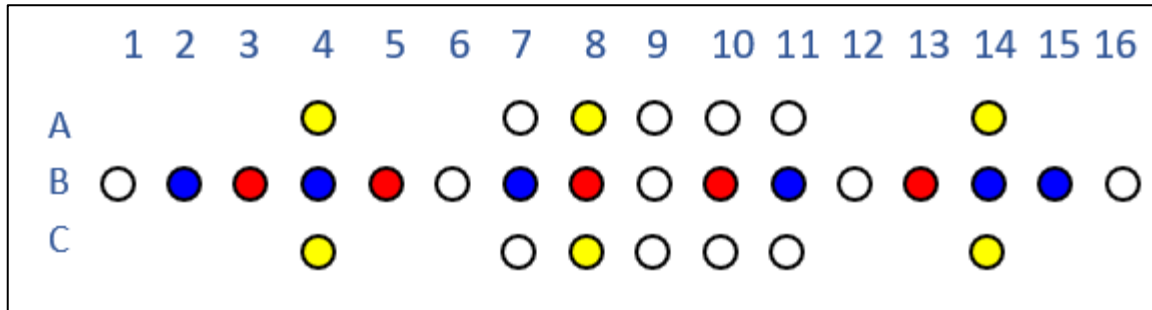


Figure 14. Test section ramp insert pressure taps used for Configuration 3 (blue), 4 (blue), 5 (yellow), and 6 (red).

(blue), 5 (yellow), and 6 (red). Only 5 pressure taps were used for Configuration 6 as a leak could be heard when sensor #5 was connected to any of the ports, and so sensor #5 was not used.

As was done for the nozzle characterization, ten test points of 2-3 seconds each were recorded for each configuration. The DC voltages were recorded for the Configuration 3, 5, and 6, test points. The AC voltages were recorded for Configuration 4 test points.

4.5. Schlieren and Shadowgraphy Imaging

A Z-type Schlieren set up around the tunnel allowed for the streamwise translation of the Schlieren system. For more details of Schlieren-based optical setup, please see background. The system required minor alignment occasionally and small amounts of manipulation to capture the desired field of view. The knife-edge was set in place of the conjugate plane of the light source to partially cut off light to introduce diffraction and thus increase sensitivity. When Shadowgraphy was performed, this knife-edge was simply removed.

The camera settings (shutter speed and ISO) were adjusted to minimize the exposure duration while still capturing consistent error-free images. Since the DSLR camera used was not intended for high-speed imaging, the shutter was limited to around 1/1000Hz.

5. ANALYSIS OF RESULTS AND DISCUSSION

5.1. Kulite Calibration

The Kulite pressure taps were first calibrated prior to any data collection following the above procedure. The calibration results were used to transform the collected voltage to pressure exerted on the individual pressure taps. The calibration results are presented in Figure 15 below.

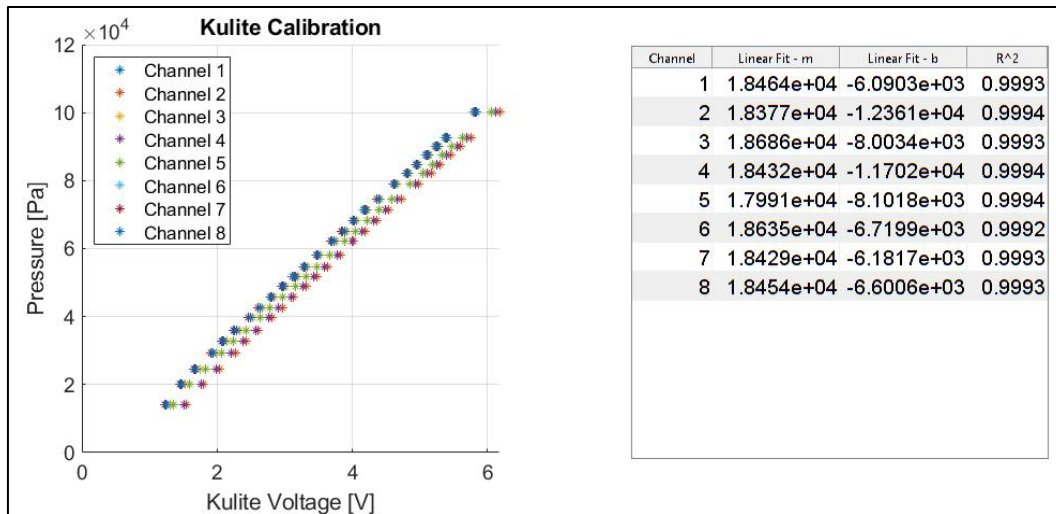


Figure 15. Kulite calibration results and table showing linear regression results for each of the 8 channels.

The corresponding slope and y-intercepts of the linear regression between voltage and pressure were reported on the right side in Figure 15. Overall, all Kulite channels showed excellent linearity in voltage-pressure correlation. Specifically, the goodness-of-fit measurements were all above 99.92%. The data demonstrated some nonlinearity in the low voltage/pressure region. Because the localized pressure within the nozzle and the test section did not reach low enough values for them to be relevant, the majority of those points were excluded from the calibration, including the plot shown above. This was also evident by the non-zero y-intercepts of the linear regression. Note that the measurements collected during the experiments were far away from this region and the nonlinearity had minimal impact during post processing.

5.2. Nozzle Characterization: centerline

The centerline characteristics of the Mach 2 nozzle were first evaluated. The geometry, specifically the area ratio and their corresponding locations, were given prior to the experiment. These were used to calculate the expected Mach number as well as pressure ratio (with respect to throat pressure), as seen in Figure 16.

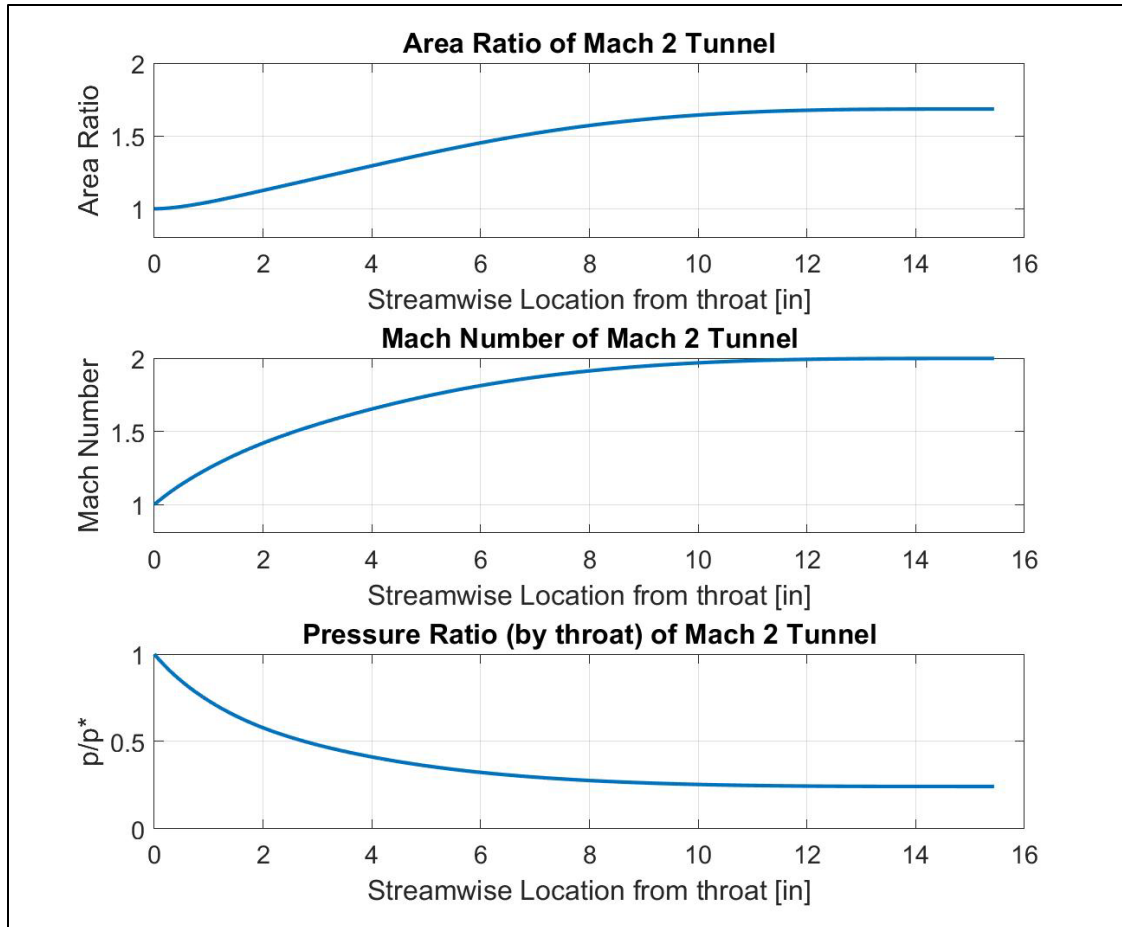


Figure 16. Area ratio, Mach number, and Pressure Ratio at distances up to 15 inches from the first throat in the tunnel

In order to verify the performance of the Mach 2 nozzle, pressure taps were placed at all locations on the nozzle centerline between the throat and the test section. Due to the limited number of the Kulites available, two separate configurations were stitched together to evaluate the entire nozzle. The pressure data from each configuration were normalized by their corresponding throat pressure for the stitching to be valid.

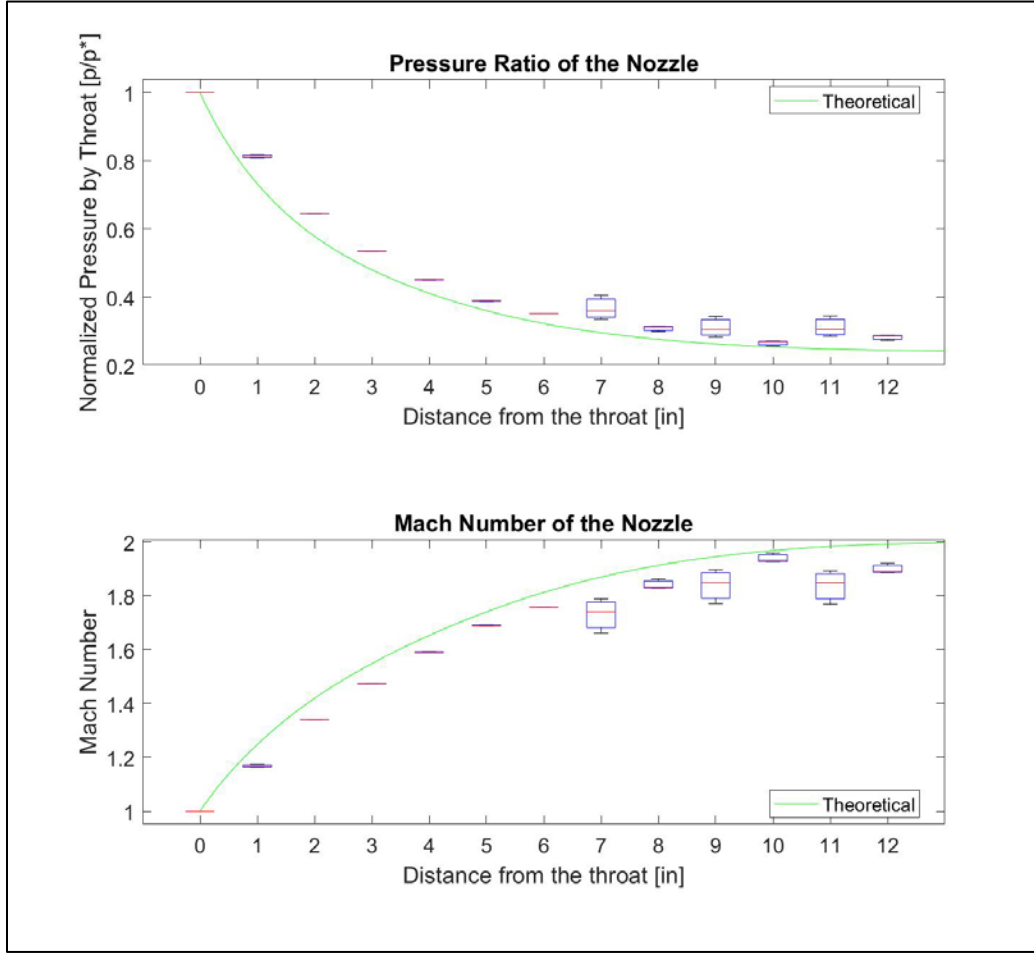


Figure 17. Nozzle pressure ratios and Mach numbers determined from Kulite pressure sensor data

The resulting pressure ratios were then used to calculate Mach number at the individual Kulite pressure sensor, using isentropic relations. The pressure ratio as well as Mach number can be seen in Figure 17 above. There were very small fluctuations between trials overall. The experimentally collected pressure ratio and Mach number also showed very good agreement with the expected values calculated from the nozzle geometry. Sensors 5, 6, and 7 showed a larger variation in the recorded data at pressure taps 7, 9, and 11, which were part of Configuration 2. These variations are discussed further in 5.7 Sources of Error and Limitations.

5.3. Ramp Characterization: Centerline

The centerline characteristics of the 20° ramp were then investigated. The pressure taps were placed at almost all centerline locations of the ramp insert. Similar to the nozzle characterization, this was done by stitching two configurations. Each configuration was scaled by their corresponding throat pressure before stitched together in Figure 18.

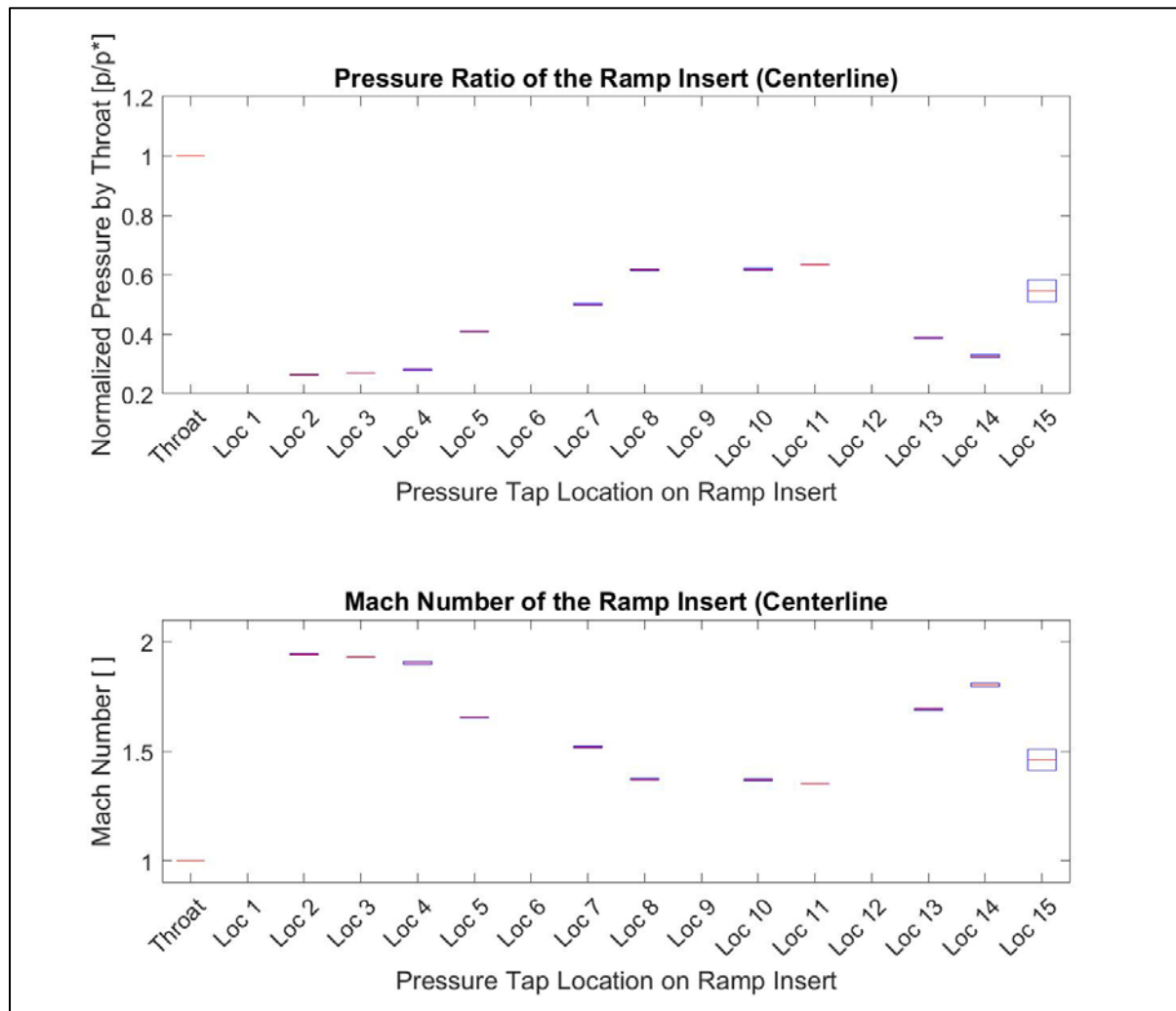


Figure 18. Pressure Ratio and Mach number along centerline of the ramp insert

Similar to the nozzle, the ramp showed an insignificant number of fluctuations of pressure ratio as well as Mach number. The only exception was at location 15 where the fluctuation was much larger than any other locations. This was likely due to the oscillatory nature of the shock wave boundary layer interaction at this location. For more details, see error analysis in the later section.

5.4. Ramp Characterization: Spanwise Variation

Once the centerline performance of the nozzle and the ramp were characterized, spanwise variations were investigated. Specifically, three sets of data were collected to capture the spanwise variations at three different streamwise locations (location 4, 8, and 14). Figure 19 below demonstrates the distribution of the pressure ratio as well as Mach number along the span of the aforementioned three locations.

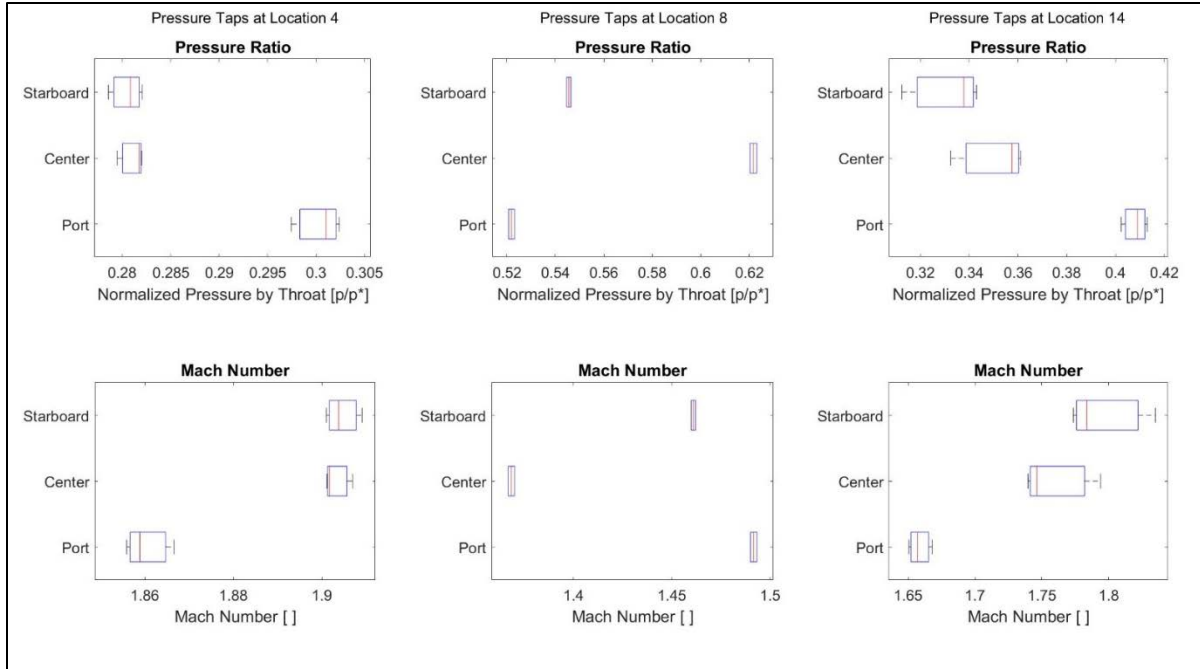


Figure 19. Spanwise pressure ratios and Mach numbers at locations 4, 8, and 14

Location 4 corresponded to the location just before the ramp. Location 8 corresponded to the corner of the ramp and Location 14 corresponded to the end of the ramp. Strong spanwise variations could be observed at the corner of the ramp where the starboard and port side of the tunnel showed smaller pressure ratios and correspondingly, higher Mach number. However, this effect was not in the other two locations. This may be caused by the imperfections of the nozzle geometry and/or the ramp geometry. More details can be found in the error analysis section.

5.5. Shockwave boundary layer interaction oscillation

Since the angle of the ramp was sufficiently large to cause the induced shockwave to detach, shockwave boundary layer interaction was of interest to be investigated here. Specifically, the stand-off or separation distance, denoted as L_{sep} . The separation bubble within this distance experienced intense expansion and contraction, causing unsteady motions within the flow. This could be seen as the separation distance oscillating. In order to capture this oscillatory motion, the AC signals from the Kulite pressure sensors were recorded. Fast Fourier Transformation was performed on the AC signals to extract any dominant frequency, as seen in Figure 20. The sample frequency was 25000 Hz and each window contained 50 data points smoothed using a moving mean technique. However, a single dominant frequency was not obvious enough to be extracted. This was likely due to the damping effect of the pressure tap line. Nonetheless, oscillations in the range of low hundred Hertz were observed in the figure and are in good agreement with [2].

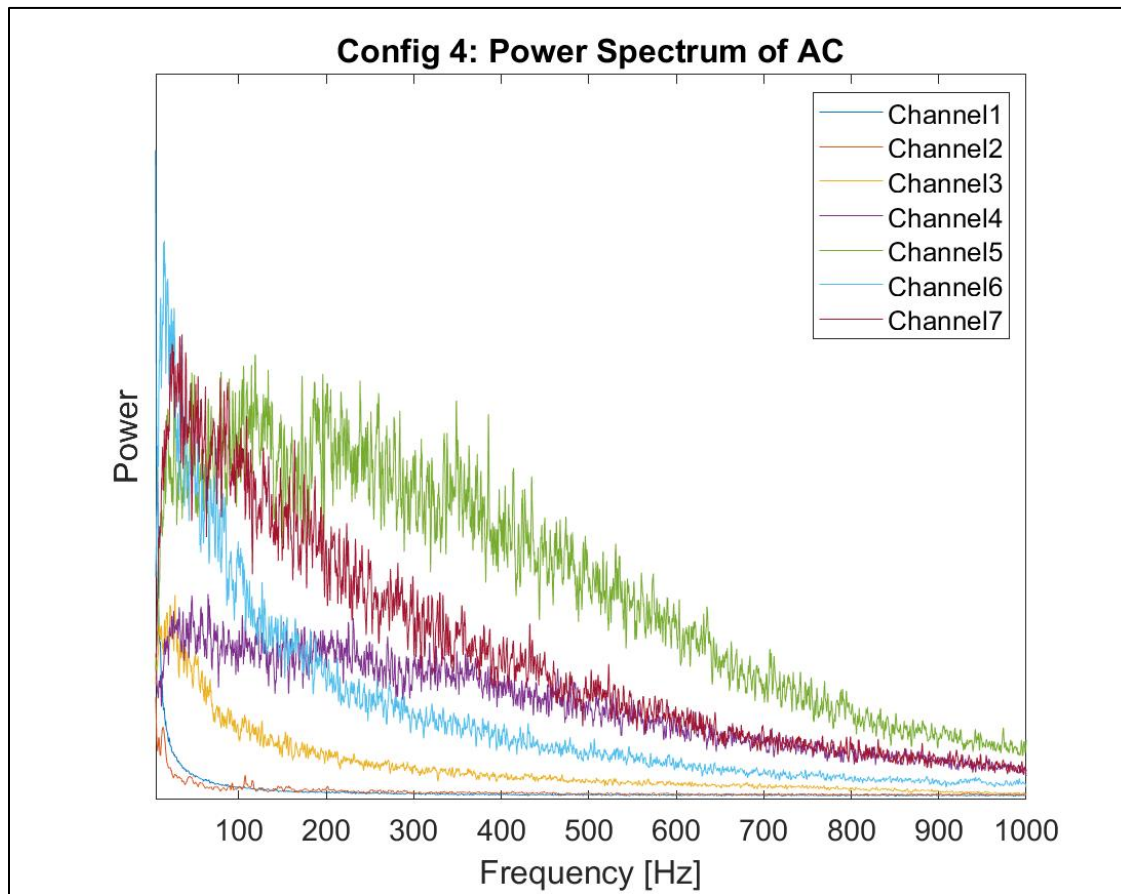


Figure 20. Fast Fourier Transformation of the AC

5.6. Schlieren and Shadowgraphy Imaging

The Schlieren and Shadowgraphy images (Figure 22 and Figure 21 respectively) were captured using the DSLR camera. Background subtraction was performed on the Shadowgraphy image to enhance contrast and get rid of window imperfections.

These flow structures can be observed with varying levels of clarity on both the Schlieren and shadowgraphy images, but for clarity, they have only been identified once each in the figures. The Schlieren image (Figure 21) shows the expected detached, oblique shock in front of the ramp, as well as the subsequent expansion fan at the top of the ramp. Between the two, a separation bubble can be seen as a lighter area under the separated flow, which shows up as a darker region just downstream of the separated shock before the expansion fan. The annotations on the shadowgraph (Figure 22) label the detached, oblique shock as well as the reflected shock and their triple point (point of intersection). This reflected shock could be problematic for certain experiments run in a supersonic tunnel, but the tunnel would have to be

significantly larger to avoid the interference of the reflected shock. The shadowgraph also shows a weak shock that was a result of the rear-facing step in the wind tunnel where the tunnel insert is installed. In both the shadowgraph and Schlieren images, the shocks do not appear as a single crisp line but instead appear to be made of multiple overlapping or blurred shocks. This thickness is proof that the flow is indeed three-dimensional as it indicates the spanwise variations in the shocks.

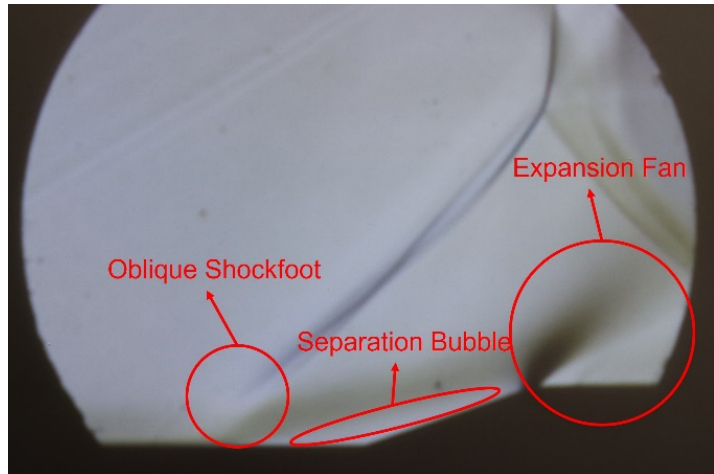


Figure 21. Schlieren image capturing the shockwave and expansion fan caused by the flow around the ramp at Mach 2.0

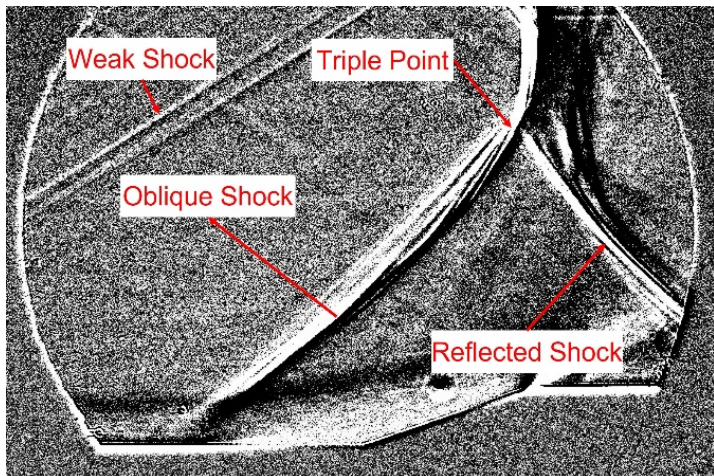


Figure 22. Shadowgraphy image with background subtraction. Note the thickness of all shocks due to three-dimensionality. Also note the weak shock tripped by the rear facing step of the tunnel insert

5.7. Sources of Error and Limitations

Some errors were found in the collected results. Specifically, specific pressure tap channels gave much more uncertainty, i.e., variance, when compared to others. This might have been caused

by a leak in the pressure tap which contaminated downstream pressure tap as well. For example, channel 5 showed drastically different values in certain configurations during the experiment. This effect propagated downstream can also be seen in channel 6 and 7. Note that in configuration 6 where locations along the centerline of the ramp were investigated, channel 5 exhibited an even larger variance and was audibly leaking, therefore it was excluded so that channel 6 and 7 were not affected.

The nozzle and ramp also showed signs of imperfection. The nozzle performance was characterized using test point data from Configuration 1 and 2. The results indicated that the flow did not quite reach Mach 2 but peaked around 1.95. Due to the design of the tunnel, there was a small backward facing step when the flow travelled into the test section. Furthermore, the ramp used in the experiment had scuffs and scratches. The aforementioned two factors could have tripped undesired oblique shocks.

5.8. Lessons Learned

In order to improve the quality of the flow, and in turn, the data collected in the future, several improvements could be made. First, pressure taps could be machined into the test article such that the Kulite sensors could be hooked up to locations that are close to each other without interference. Currently the thickness of the tubing and closeness of the taps prevents adjacent taps from being used simultaneously. Doing so would minimize the likelihood of pressure tap leak and allow more accurate pressure measurements.

Moreover, the pressure measurements contained dynamic artifacts due to the long tube connecting the pressure taps to the Kulite transducer. The long tubes acted as settling chambers and damped out any oscillations presented in the pressure measurements. This could be addressed by using shorter tubes or directly implementing the Kulite sensors near the pressure taps.

Finally, the six configurations tested were not enough to record data from all available pressure taps, given the limited number of Kulites available. Additional insights into the data may have been possible if data from all pressure taps were available, requiring either more time or more sensors.

6. CONCLUSIONS

This experiment aimed to investigate and characterize the supersonic flow (Mach 2) around a 20° ramp. The objectives were to utilize Kulite pressure sensors and Schlieren-based optical flow visualization techniques to qualitatively and quantitatively describe the shockwave boundary layer interaction. Schlieren and Shadowgraphy images were recorded with fast shutter speeds in attempts to freeze frame the flow. They showed clear separated oblique shock upstream of the

ramp as well as the closed interaction, i.e., the separation bubble where the fluid was trapped within. Pressure sensors were placed along centerline locations of the nozzle itself to verify the supersonic flow conditions prior to the test section. The nozzle was able to achieve flow very close to the intended Mach number and provided a good basis for the experiment. The pressure taps were then placed on the ramp at both centerline locations and various spanwise locations. The recorded pressure demonstrated some three-dimensionality to the flow where the side wall boundary layer had played a large role in the near wall flow. The three-dimensional appeared to be asymmetrical, suggesting that there were imperfections within the nozzle or ramp designs.

7. REFERENCES

- [1] J. D. Anderson, *Fundamentals of aerodynamics*, 5th ed. McGraw-Hill, 2011.
- [2] N. T. Clemens and V. Narayanaswamy, “Low-Frequency Unsteadiness of Shock Wave/Turbulent Boundary Layer Interactions,” *Annual Review of Fluid Mechanics*, vol. 46, no. 1, pp. 469–492, 2014, doi: [10.1146/annurev-fluid-010313-141346](https://doi.org/10.1146/annurev-fluid-010313-141346).
- [3] M. Erenkil and D. Dolling, “Correlation of separation shock motion with pressure fluctuations in the incoming boundary layer,” *AIAA Journal - AIAA J*, vol. 29, pp. 1868–1877, Nov. 1991, doi: [10.2514/3.10812](https://doi.org/10.2514/3.10812).
- [4] “Schlieren photography,” *Wikipedia*. Jan. 31, 2022. Accessed: Mar. 04, 2022. [Online]. Available: https://en.wikipedia.org/w/index.php?title=Schlieren_photography&oldid=1069029511
- [5] A. Roshko and H. W. Liepmann, *Elements of Gasdynamics*. Wiley, 1957. Accessed: Mar. 04, 2022. [Online]. Available: <https://engineering.purdue.edu/~aae520/Schlieren-appA-L&R-p.pdf>
- [6] J. Jewell, Class Notes, “Supersonic Wind Tunnel”, AAE 52000, College of Engineering, Purdue University, West Lafayette, IN, Jan 2022.